Design Optimization of a Slotless PM Brushless Motor with Helical Edge Wound Laminations for Rim Driven Thrusters

S. M. Sharkh, S. H. Lai

Abstract—**This paper discusses the analysis and design of a very thin slotless PM brushless motor whose stator laminations are manufactured from a single strip of steel that is edge wound into a spiral (like a "Slinky") and then fitted over the windings that are preformed on the outside surface of a non-conducting former. Analytical and finite element analysis (FEA) are used to determine the constrained optimum dimensions of a motor used to drive a rim driven thruster in which the motor rotor is fitted onto the rim of the propeller and the stator is encapsulated in the thin Kort nozzle of the thruster. The paper describes the fabrication of a demonstrator motor and presents experimental results to validate the theoretical calculations. Experimental motor performance results are also reported and compared with those of a slotted motor that fits within the same active radial dimensions as the slotless motor. The slotless motor, which has longer active length and endwindings, and thicker magnets than the slotted motor, was found to be less efficient and more expensive (prototype cost) than the slotted machine.**

***Index Terms*—Slotless brushless PM motor, edge-wound laminations, rim driven thruster.**

I. Introduction

IN rim or tip driven thrusters and marine turbine generators such as those illustrated in Fig. 1 and Fig. 2 [1-14], the machine active components need to fit within the small space in the duct or Kort nozzle that surrounds the propeller. The duct ideally needs to be relatively thin to minimize hydrodynamic drag forces and achieve good thrust efficiency. Although demonstrator rim driven thrusters were built using induction [5] and switched reluctance machines [11], PM machines are bests suited to this application as they are more efficient and can be designed to have a large number of poles and hence be very thin. They are also tolerant of having a large airgap that is needed to accommodate stator and rotor encapsulation layers.

The manufacture of such radially thin machines poses several practical challenges. For example, the 50 mm propeller diameter thruster shown in Fig. 2 [1] has a lamination yoke thickness of 1.25mm and teeth that are only 1.5 mm wide. This makes lamination production and handling challenging and costly.

Fig. 1. Photograph of a commercial rim-driven thruster (courtesy TSL Technology Ltd).

This paper investigates the design and performance of an alternative brusless PM motor topology that has the potential to overcome these difficulties. In this topology the stator laminations of the slotless motor are manufactured from a single strip of steel that is edge wound into a spiral like a "Slinky". The helical laminations are then fitted over the windings that are preformed on the outside of a non-conducting former. A brief description of the motor and preliminary performance results were published in a previous conference paper by the authors [14]. This paper presents the details of the methodology used to optimize the design of the motor using analytical and FEA methods. The paper also elaborates the lamination fabrication process and describes the construction of a demonstrator motor for a small rim driven thruster. Experimental performance results are reported and compared with those of a slotted motor that fits within the

S. M. Sharkh is a senior lecturer at the University of Southampton, School of Engineering Sciences, Highfield, Southampton SO17 1BJ, UK (corresponding author) phone: +442380593397; fax: +442380593230 (e-mail: suleiman@soton.ac.uk).

S. H. Lai currently works as a Process Support Engineer with Applied Materials South East Asia Pte Ltd in Singapore (email: shuhau.lai@gmail.com).

same active radial dimensions as the slotless motor. The experimental results are also compared with theoretical calculations.

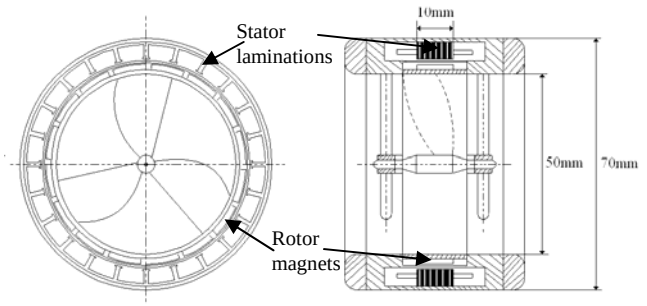

Fig. 2. A drawing of a rim driven thruster designed by the Authors [1]

II. Motor Analysis and Design

A. Preliminary Analytical Design Optimisation

An analytical method was used to analyze candidate motor designs and determine the initial constrained optimal dimensions of the motor such that maximum efficiency is achieved. The motor for the rim-driven thruster described later in this paper is required to fit within a certain volume inside the thruster nozzle, with constraints on the inner rotor radius R_r and the outer stator lamination radius R_o, and overall length L_o. The gap between the magnets and the stator bore, which needs to be relatively large as mentioned earlier, is also constrained by mechanical design requirements. The objective is to determine the dimensions of a machine that fits within these constraints such that the efficiency is maximized, for given torque T_p and speed ω. The torque value takes into account bearing friction loss as well as propeller torque.

For given available motor volume and current density, efficiency is determined by three main parameters, namely magnet thickness, number of poles and active length. Arguably, current density is also another parameter that is determined by the degree of cooling, which is a function of the thickness of the windings, but for feasible designs (designs that fit within the available space) of the machine under study, which has radially thin windings, the maximum permissible current density was found to be approximately constant. The magnet outer diameter needs to be adjusted such that the remaining space for the rotor yoke is sufficient to carry the flux at a suitable working flux density. Similarly, the radial thickness of the winding is constrained by the need to have sufficient stator yoke thickness to carry the flux at a suitable working flux density.

The design procedure, which was implemented with the aid of a computer program, was as follows. An initial active length, number of poles and magnet thickness were estimated based on simple hand calculations similar to those discussed in [17]. A first guess of the outer diameter of the magnet is also made. The airgap and magnet flux distribution was determined by solving Laplace's and Poisson's equations of the scalar magnetic potentials φ_I and φ_{II} in the airgap and magnets, respectively, assuming parallel magnetized magnets and a suitable value for magnet width to pole pitch ratio α as described in the Appendix, in which the definitions of most of the mathematical symbols below are also included.

The no-load flux carried by the rotor yoke was calculated by integrating the flux density vector in equation (A25) over half a pole pitch of the rotor steel outer surface. Assuming an appropriate maximum no-load working flux density B_{satr} in the rotor, the rotor yoke thickness y_r can be calculated to be

$$y_r = \frac{1}{B_{satr}} \int_0^{\frac{\pi}{2p}} B_{rII}(R_r, \theta) R_r d\theta \tag{1}$$

The rotor inner radius was then calculated by subtracting the magnet thickness and rotor yoke thickness from the assumed magnet outer radius. If the calculated inner rotor radius was different from the given value R_r, then the outer diameter (OD) of the magnet was changed using an optimization routine, which minimized the square of the difference between the calculated inner radius and the given value R_r, and the above calculations were repeated. If the new value for the OD of the magnet was found to be greater than the given outer diameter of the motor, then the number of poles was increased and the above calculations were repeated. If the magnet OD however was less than the given stator OD, the thickness of the stator yoke y_s was calculated using equation (2) below, such that the no-load working flux density in the stator laminations the does not exceed an appropriate value B_{sats},.

$$y_s = \frac{1}{B_{sats}} \int_0^{\frac{\pi}{2p}} B_{rI}(R_s, \theta) R_s d\theta \tag{2}$$

The thickness of the winding is then calculated. The design was rejected if the winding thickness was below a certain value or negative, and the number of poles was increased again till the radial space available for winding was above a set threshold dictated by mechanical design considerations. Next the endwiding overhang axial length was calculated, which was subtracted from L_o to calculate the active length L. If L was negative, the design was rejected and the number of poles was increased and the calculations were repeated.

Once a feasible motor design, i.e. a design that fits within the dimensions constraints, was obtained, further analysis was carried out to determine losses and efficiency. No-load iron losses P_{Fe} were estimated from empirical data for the lamination material used,

$$P_{Fe} = (p_c + p_h + p_e) \times M_{Fe} \tag{3}$$

where M_{Fe} is the mass of the stator laminations, and p_c, p_h, p_e are the eddy current, hysteresis and excess power loss densities. For each flux harmonic n, the different components of loss are calculated using the following formulae, variants of which could be found in many textbooks and papers on the subject such as [17]:

$$\begin{aligned} p_{nc} &= K_c B_n^2 f_n^2 \\ p_{nh} &= K_h B_n^2 f_n \\ p_{ne} &= K_e B_n^{1.5} f_n^{1.5} \\ K_c &= \frac{\pi^2 \tau \sigma}{6\rho} \end{aligned} \tag{4}$$

where σ, τ, ρ are the conductivity, thickness and density of the laminations, respectively, and K_h and K_e are constants determined from empirical data.

Neglecting saturation, the electromagnetic torque exerted on the rotor due to the interaction of stator current and rotor magnetic fields is given by:

$$T = -2pL\int_A \mathbf{r}\times(\mathbf{J}\times\mathbf{B}_I)dA \tag{5}$$

where **J** denotes the winding current density vector and L is the active length of the machine. A is the cross-sectional area of the coils under a pole pitch. In polar coordinates the magnitude of the instantaneous electromagnet torque can be readily shown to be given by,

$$T = 2Lp\int_{-\frac{\pi}{2p}}^{\frac{\pi}{2p}}\int_{R_{w1}}^{R_{w2}} JB_{rI}\,r\,dr\,d\theta \tag{6}$$

where R_{w1} is the inner radius of the winding and R_{w2} is the outer radius of the winding. A further approximation may be made if the winding is radially very thin with a thickness t_w=R_{w2}-R_{w1}, and the radial variation of flux density is negligible,

$$T = 2Lpt_w\int_{-\frac{\pi}{2p}}^{\frac{\pi}{2p}} JB_{rI}(R_w,\theta)\,d\theta \tag{7}$$

where R_w is the average winding radius.

The motor was assumed to be driven by a brushless DC trapezoidal drive. An ideal quasi-squarewave current was assumed for the purpose of the analytical optimization studies as shown in Figure 3. The winding was assumed to be a lap, fully pitched, Y-connected winding (see Fig. 7 and 8), and hence only two-thirds of the winding i.e. two of the phases carry current at any one time. The winding current distribution opposite a magnet under the maximum torque condition will be symmetrical about the magnet's axis, being constant between –60 electrical degree and +60 electrical degrees either side of the axis and zero otherwise. Average electromagnetic torque T_{em} is calculated by averaging the instantaneous torque values calculated over the 60 electrical degrees of rotation during which the current spatial pattern remains fixed.

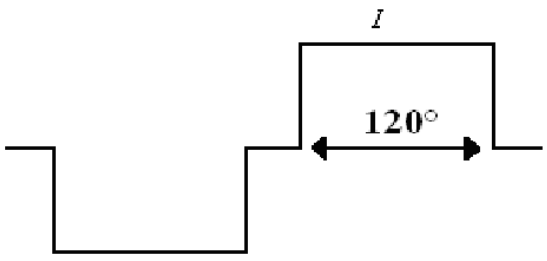

Fig. 3. Ideal quasi-aquarewave waveform

The average electromagnet torque produced by the motor T_{em} is estimated as

$$T_{em} = T_p + \frac{P_{Fe}}{\omega} \tag{8}$$

The actual electromagnetic torque needs to be slightly higher than this to allow for the increased iron loss caused by the armature reaction flux. But for the motor under consideration, armature reaction and associated increase in iron loss was found to be not significant, based on FEA results.

Using a discrete form of (7) the current density in the windings was estimated for the required average torque [15]. Copper losses were then calculated in the usual manner by estimating the mean length of turn (MLT) of a coil, and hence the total wire length of a phase, assuming that each coil has 1 turn to start with. The number of turns was later adjusted depending on the operating voltage, as discussed in the following section. The cross-sectional area of the wire was estimated by multiplying the available space with an appropriate fill factor (FF). The phase resistance R was then calculated in the usual manner assuming copper resistivity at an initial estimated working temperature. Copper loss is calculated using the following equation,

$$P_{Cu} = 2I^2R \tag{9}$$

where I is the peak phase current calculated by multiplying the copper current density by the copper cross-sectional area of a current carrying coil (assuming 1 turn per coil as discussed above).

A thermal network model, using copper and iron losses as inputs, was used to calculate the temperature of the winding, and accordingly the phase resistance is recalculated at the new temperature, and the thermal network calculations were iterated until the change of the estimated winding temperature became less than 1°C. If the winding temperature was higher than a maximum permissible temperature, the design was rejected and the number of poles was increased and/or magnet thickness was reduced and the calculations were repeated.

The efficiency of the machine was estimated as

$$\eta = \frac{T_p\omega}{T_p\omega + P_{Cu} + P_{Fe}}\times 100 \tag{10}$$

To gain an insight into the design optimization process, motor efficiency for given torque and speed was calculated for a range of feasible number of poles, magnet thicknesses, active lengths and α as illustrated in Figs. 4, 5 and 6, for given winding current density. For given number of poles, active length and α in Fig. 4, the efficiency initially increases as the magnet thickness and the magnetic loading are increased. But further increase of magnet thickness beyond a certain value results in a decrease of efficiency due to the reduction of the space available for the windings and the increased copper loss.

In Fig. 4, for a given magnet thickness, increasing the number of poles leads to i) a reduction of the rotor yoke and stator yoke steel thicknesses and thus an increase in the space available for the windings, ii) a reduction in the length of the endwinding, iii) an increase of the proportion of flux leakage between neighbouring magnets and a net reduction in the average flux density in the machine. Both i) and ii) lead to a reduction in the winding resistance and corresponding copper loss, but iii) leads to an increase in the winding current or electric loading, with a corresponding increase in copper loss, to compensate for the reduction in magnetic loading. The

significance of these two opposing effects depends on magnet thickness. For thin magnet designs (3mm and 4mm magnets in Fig. 4), the effect iii) i.e. leakage flux between neighbouring magnets was found to be more dominant, thus favouring low number of poles. But for designs with thick magnets (6 mm case in Fig. 4), increasing the number of poles actually improves the efficiency, which suggests that i) and ii) are more significant. Between the extremes of thin and thick magnets, the picture is mixed and there is an optimum number of poles at which efficiency is maximum.

The effect of active length and α is more straightforward. As expected, the efficiency improves as the active length and α are increased as illustrated in Figs. 5 and 6.

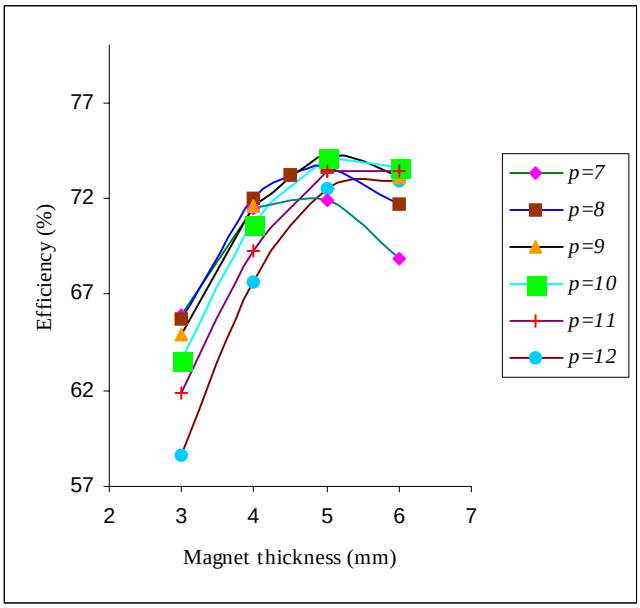

Fig. 4. Efficiency versus magnet thickness and number of poles with L=25mm, α=0.83.

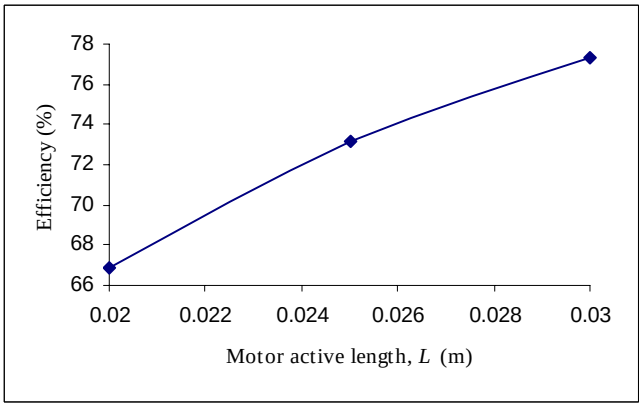

Fig. 5. Efficiency versus active length for a design with 16 poles and 4.5 mm thick magnets, α=0.83.

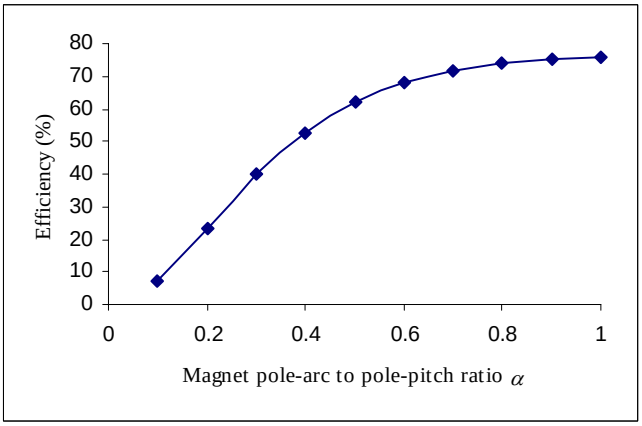

Fig. 6. Efficiency versus α

B. *Calculation of the number of turns*

An equivalent circuit simulation model of the motor and the driving inverter as shown in Fig. 7 was used to further analyze near optimum designs. This enabled current waveforms to be calculated and helped determine the number of turns for given power, speed and DC link voltage.

The open circuit back emfs E_A, E_B and E_C were calculated as follows. The flux ψ linking a phase coil was calculated by integrating the radial component of flux density (A21) over the cylindrical surface of the coil at the average radius of the winding R_w, which as expected for the motor under consideration was almost identical to the integral evaluated at the stator bore over a coil pitch.

In the stator frame of reference the angle β is related to the angle θ in the rotor frame of reference by the following equation,

$$\beta = \theta + \theta_o + \omega t \tag{11}$$

Where θ_o is an initial angle when β=0, which depends on the commutation angle, i.e. the degree of phase advance, and the spatial location of a phase coil. From equation (A21) the radial flux density distribution at the winding average radius is then given by

$$B_{rl}(R_w, \beta) = \sum_{n=1,3,5...}^{\infty} B_n \cos np(\beta - \omega t - \theta_o) \tag{12}$$

where $B_n = K_B(n) f_{Br}(R_w)$. The flux linking a stator coil is then given by

$$\psi = \int_{-\frac{\beta_c}{2}}^{\frac{\beta_c}{2}} B_{rl}(R_w, \beta) R_w L d\beta \tag{13}$$

where β_c is the coil pitch angle. The emf E in a phase with N turns in series can be calculated using Faraday's law,

$$E = \frac{-dN\psi}{dt} \tag{14}$$

It can be shown that a phase emf is given by

$$E = \sum_{n=1,3,5,...}^{\infty} 2NB_n R_w L \omega K_{pn} \sin np(\omega t + \theta_o) \tag{15}$$

where

$$K_{pn} = \sin np\frac{\beta_c}{2} \tag{16}$$

The phase inductance element L_{ph} in Fig. 6 was calculated as

$$L_{ph} = L_s - M + L_{end} \tag{17}$$

where L_{end} is the endwinding inductance estimated using expressions that can be found in [17]. The self and mutual airgap inductances L_s and M were calculated by evaluating the armature reaction field using a 2D scalar potential Laplace equation polar coordinate model. A solution of the armature reaction field can be found in [18], and hence details of the solution will not be repeated here to avoid duplication.

Circuit simulations were carried out using Matlab SimpowerSystems Blockset, using hot resistance values. The instantaneous electromagnetic torque produced by the machine was calculated as

$$T = \frac{1}{\omega}(E_A i_A + E_B i_B + E_C i_C) \tag{18}$$

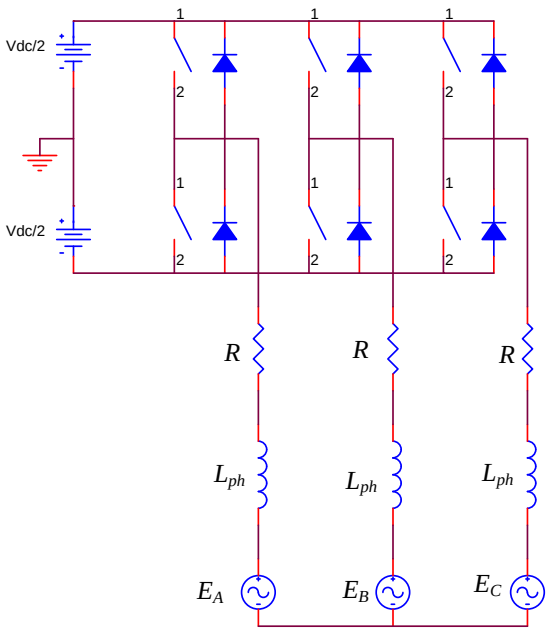

Fig. 7. Equivalent circuit simulation model of motor and inverter

For a given DC link voltage, the number of turns was adjusted and the circuit simulations were repeated until the average torque at least equaled the required value. The resistance and inductance values were adjusted in proportion to the square of the number of turns. The rms value of the current waveforms was also evaluated and the copper losses and efficiency were also recalculated based on the more realist waveforms. For the motor reported here, the difference between the average values of torque and efficiency calculated using ideal currents and those obtained from circuit simulation were found to be small.

C. FEA Analysis

Feasible designs were further analysed using two-dimensional transient finite element analysis incorporating rotor motion and external 3-phase inverter circuit as described in [1]. Fig. 8 shows the geometry of the FEA model and the flux distribution in a two-pole section of a candidate motor design at a particular instant in time.

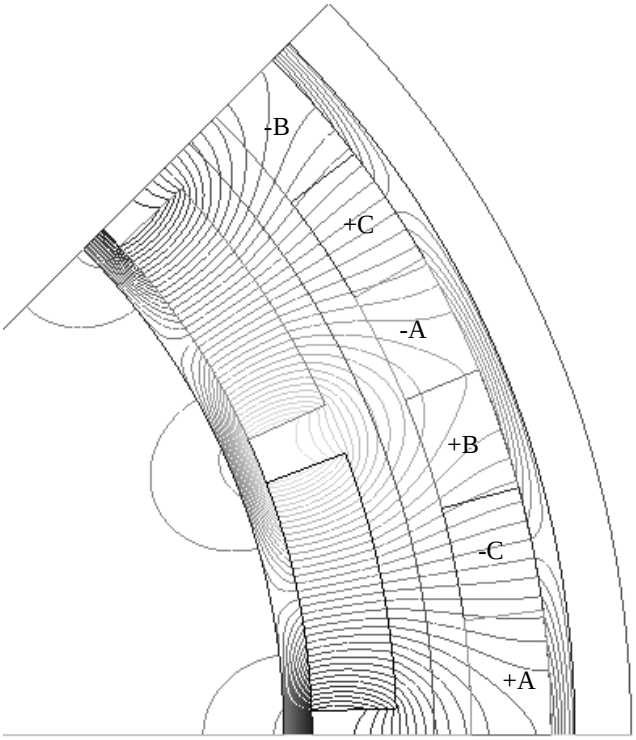

Fig. 8. Winding configuration and FEA flux distribution in a candidate motor design

Fig. 9 compares the flux density computed by both FEA and analytical methods. The analytical values were found to be higher than the FEA values. This can be explained to be due to the assumption of infinite steel permeability in the analytical solution, which neglects the mmf drop along the steel path. As a result of this, the FEA computed emf, torque, core loss and efficiency were found to be slightly lower than the analytical values. The FEA computed core loss for example was 7W compared to 8W that was calculated analytically, and the efficiency computed using FEA was 71% compared to 73% calculated using the analytical method.

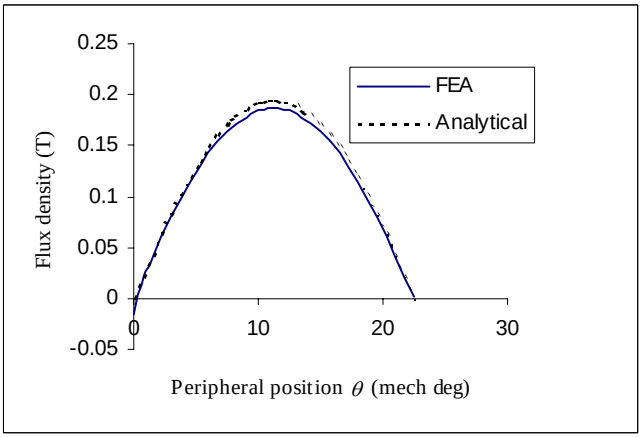

Fig. 9. Analytical and FEA flux density at stator bore

III. Description of the Demonstrator Motor

Table 1 presents a summary of principal motor parameters as manufactured, compared with a slotted motor that fits within the same radial dimensions. Although the optimum value of the number of poles of the slotless motor was found to be 20, with α=1 and magnet thickness of 5mm, the actual number of poles of manufactured motor was selected to be 16 poles with a magnet thickness of 4.5 mm and an α=0.833. These decisions were made based on practical considerations of availability of materials and ease of fabrication of components. But the efficiency of the selected design was only marginally lower than the optimal motor as illustrated in Fig. 4.

TABLE 1
PARAMETERS OF SLOTLESS AND SLOTTED MOTORS

Parameter	**Slotless**	**Slotted**
Stator steel thickness	1.25mm	1.25mm
Rotor steel thickness	1.5mm	1.5mm
Number of poles	16	16mm
Magnet thickness	4.5mm	3.0mm
Motor axial length	25mm	20mm
α	0.833	0.833
Stator OD	104mm	104mm
Rotor ID	73mm	73mm
Electromagnetic airgap	4mm	4mm
Nominal torque	0.68Nm	0.68Nm
Nominal speed	3600rpm	3600rpm
Efficiency at full load	71%	82%
Core loss	7W	14W
Laminations cost	£34	£50
Magnets cost	£295	£120
Windings cost	£250	£190
Encapsulation cost	£75	£20
Total cost	£654	£380

The slotted motor, which has 1.5 slots per pole per phase and concentrated windings, has a shorter active length and thinner magnets. Both motors fit within the constraints of the space available in the duct of the rim driven thruster shown in Fig 2, which has a propeller diameter of 70 mm.

A photograph of the slotless thruster motor components before assembly is shown in Fig. 10. The stator windings were wound on a former made of non-conducting, non-magnetic Derlin material with suitable properties. The former outer surface was machined to have slots to guide the windings. The former also functions as part of a water-sealed housing system for the stator having two O-rings at either end that seal the stator within an aluminium shroud.

The stator laminations were formed from a single strip of steel 0.5 mm thick and 1.25 mm wide. The strip was edge wound under tension on a mandrel that was smaller in diameter than the final diameter of the helical lamination. A helical thread-like groove was machined on the surface of the mandrel to guide the steel strip and prevent it from its natural tendency to bend flat. The wound strip was left on the mandrel for approximately 12 hours to even stress distribution, before removing it from the threaded small diameter mandrel and clamping it on a mandrel of the correct larger diameter. The whole assembly was then normalised at a high temperature of 580 ^{o}C for two hours.

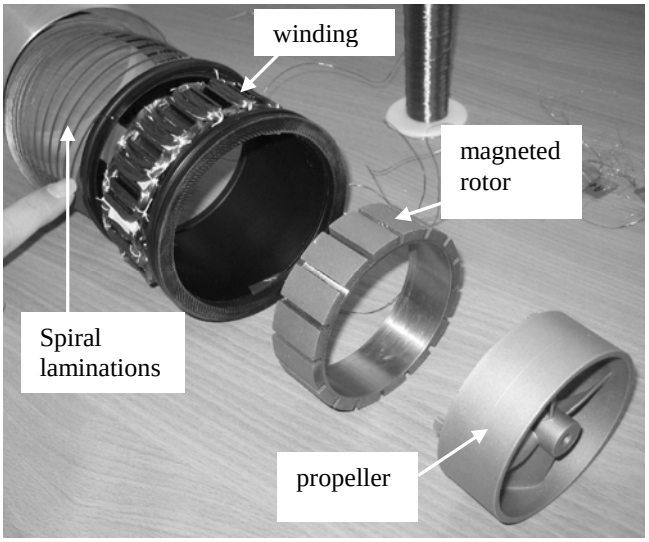

Fig. 10. Photograph of motor before assembly

The helical laminations were then fitted and tightened over the slot liner covering the windings. Insulating varnish was subsequently applied to glue the assembly of laminations and windings and improve thermal conductivity. The whole assembly was then sealed in the aluminium shroud, which forms the outer surface of the thruster and supports the bearing assembly spider. The propeller was fitted inside the rotor ring and the whole rotor assembly was potted in epoxy.

IV. Test Results

Tests were carried out to validate the computed results and to assess the performance of the machine compared to the slotted design. Testing was carried out using a general-purpose dynamometer rig to measure locked rotor torque current characteristics, emf and efficiency at different loads. Tests were also carried out on thrusters using the two motors to provide a direct comparison of performance in terms of power needed for required thrust. The measurements uncertainties were as follows: torque error = ±0.07Nm, speed error = ±0.1rpm, voltage error = ±0.01V, current error = ±0.01A, thrust measurement error = ±1N.

Fig. 11 shows a comparison of the back-EMF waveforms vs. rotor position obtained from both experimental and finite element analysis. Fig. 12 shows both experimental and finite element locked rotor torque vs current characteristics. Fig. 13 shows a comparison between experimental and FEA computed current waveforms. A good agreement between finite element and experimental results is generally observed. The experimental torque measurements at low current were generally lower than the theoretical values, but the level of confidence in the accuracy of these low current results is low as the values were close to the level of uncertainty in torque measurement.

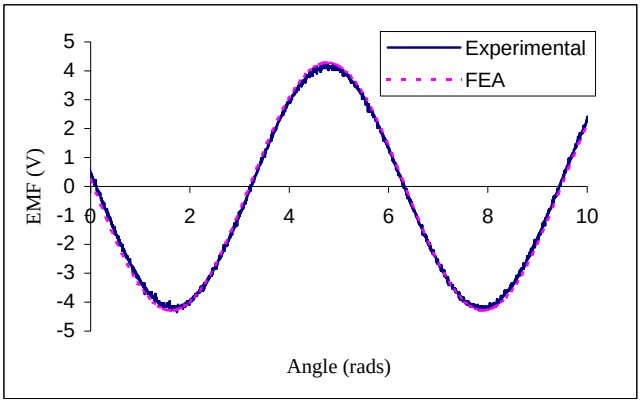

Fig. 11. Back EMF waveforms from FEA and experimental 993 rpm

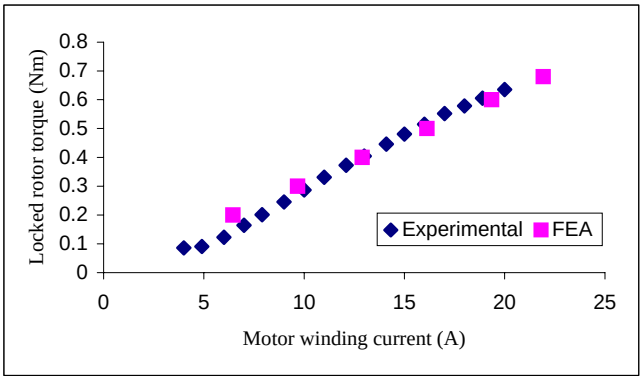

Fig. 12. Locked-rotor torque versus current characteristics

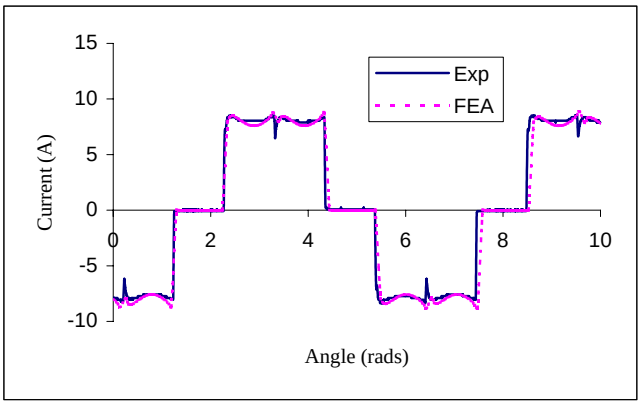

Fig. 13. FEA and experimental current waveforms at 993 rpm, 0.24 Nm

The general-purpose dynamometer rig was also used to measure the efficiency of the slotless machine, which was also found to be in general agreement with calculations, when bearing friction and windage were allowed for.

A direct comparison between the performance of the slotless and the slotted machines is illustrated in Figs. 14 and 15. Thrust was measured at bollard-pull condition. Both thrusters had the same propeller and the same external dimensions, and the hydrodynamic propeller performance of the thrusters was essentially identical as demonstrated in Fig. 14: for a given propeller speed, the output thrust was basically the same for both thrusters and the propeller torque should also be the same for both thruster. But the slotless motor was drawing significantly more power for given thrust output as shown in Fig. 15. The efficiency of the slotless design was about 11% below that of the smaller slotted motor.

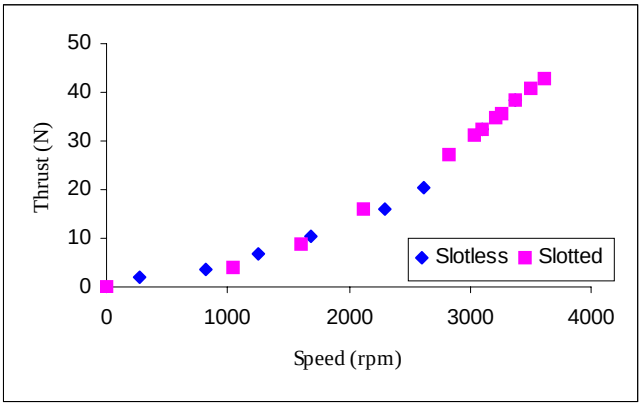

Fig. 14 Thrust vs speed

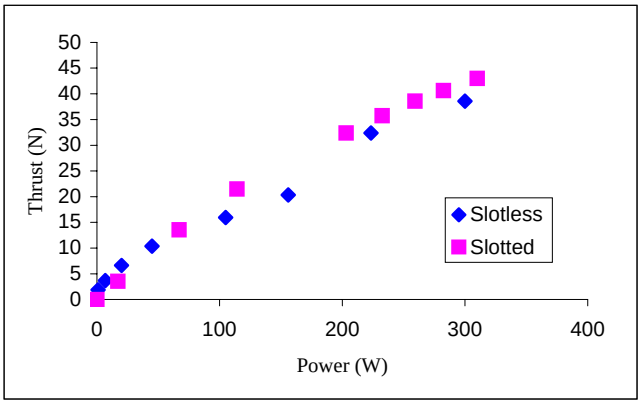

Fig. 15. Thrust vs power

Table 1 shows a comparison between the prototype costs of the slotless and the slotted motor. The cost of the slotless motor, which has more magnet material and copper, was nearly double that of the slotted machine. This increase in cost was entirely due to the increase in magnet and copper materials. Although the lamination cost was slightly cheaper, this saving was more than offset by the need for a winding former.

V. Conclusions

For the particular rim-driven thruster application and the particular demonstrator motor investigated in this paper, the proposed slotless motor topology with helical laminations was found to be inferior to an equivalent slotted motor that fits within the same radial dimensions. The slotless motor was larger and less efficient than the slotted machine. But care needs to be taken before drawing general conclusions, as in other applications and for motors with different dimensions, the picture may be different and the slotless motor design may be more favourable, especially when the motor is produced in large volumes.

The paper presented a methodology for the design of such a machine. Analytical methods based on solution of Laplace and Poisson's equations of the magnetic field in the motor gap were demonstrated to be in good agreement with FEA and experimental results.

REFERENCES

[1] Sharkh S M, Lai S H and Turnock S R. A Structurally Integrated Brushless PM Motor for Miniature Propeller Thrusters, *IEE Proc.-Electr Power Appl*, 2004,151 (5): 513-519

[2] Sharkh S M, Hughes A and Turnock S R. Design and performance of an electric tip-driven thrusters, *Proc. Instn Mech. Engrs M: J. Engineering for the Marine Environment*, 2003, 127:133-147

[3] Sharkh S M. Propulsion for AUVs, in Griffiths, G (Ed.), *Technology and Applications of Autonomous underwater vehicles*, Taylor and Francis, 2003.

[4] Sharkh S M, Morris D, Mayer L, Turnock S R, and Bahaj A S. Performance of an integrated water turbine PM generator, In: *Proceedings of IEE PEMD Conference*, Bath, UK, 2002. 486-489

[5] Brown D W, Repp J R, Taylor O S. Submersible outboard electric motor/propulsor, *Nav. Eng. J.*, 1989, 101:44-52.

[6] Holt J K and Kennedy G C. Propulsion systems for submarine vessels, US Patent:5306183, 1994

[7] Kort L. Elektrisch angertriebene Schiffsschraube, German Patent : 688114, 1940

[8] Krovel O, Nilssen R, Skaar S E, et al. Design of an integrated 100 kW Permanent Magnet Synchronous machine in a prototype thrusters for ship propulsion. In: *International Conference on Electrical Machines ICEM2004*, Cracow, Poland, 2004. 117-118

[9] Lea M, Thompson D, Van Blarcom B, et al. Scale model testing of a commercial rim driven propulsor pod, *Journal of Ship Production*, 2004, 19 (2):121-130

[10] Richards J. Further development in pod propulsion, *New Wave*, 2003, 1: 4

[11] Richardson K M, Pollock C, and Flower J O. Design of a Switched Reluctance Motor for an Integrated Motor/Propeller Unit. In: *Proceedings from the IEE Seventh International Conference on Electrical Machines and Drives*, Durham, 1995. 271-275

[12] Rolls-Royce introduces Rim Drive thruster technology, Press release published on http://www.marinelog.com/DOCS/NEWSMMV/2005nov00150.html. Accessed on 8 Jan 2005

[13] Pashias C, Turnock S R, Sharkh S M. Design optimisation of a bi-directional integrated thruster. In: Proceedings *of Propeller Shafting Conference*, Miami, 2003. 13 pages.

[14] Lai S H, Sharkh S M. Structurally integrated slotless PM brushless motor with spiral wound laminations for marine thrusters. In: *The Third International Conference on Power Electronics Machines and Drives PEMD*, Dublin, 2006. 106-110

[15] Lai S H. Design Optimisation of a Slotless Brushless Permanent Magnet DC Motor with Helically-Wound Laminations for Underwater Rim-Driven Thrusters: [Ph. D dissertation]. University of Southampton, 2006.

[16] Zhu Z Q, Howe D, Chan C C. Improved analytical model for predicting the magnetic field distribution in brushless permanent magnet machines, *IEEE Trans. Magn.*, 2002, 38 (1):229-238

[17] Hindershot J R and Miller T J E. *Design of Brushless PM Motors*, Magna Physics and Oxford Science Publications, 1994.

[18] Zhu Z Q and Howe D. Instantaneous magnetic field distribution in brushless permanent magnet DC motors, Part II: Armature-Reaction Field, *IEEE Transactions on Magnetics*, 1993, 29(1): 136-142

ACKNOWLEDGMENT

The Authors wish to thank Mr Ian Edwards for his support. They also wish to thank Mr Bryan Clarke for his help in the manufacture of the thruster. Thanks are also due to Dr Michael Yuratich of TSL Technology Ltd for providing a propeller and bearings for the demonstrator slotless thruster, an a thruster with a slotted motor.

S. M. Sharkh obtained his BEng and PhD degrees in Electrical Engineering from the University of Southampton in 1990 and 1994, respectively.

He current works as a senior lecturer in the School of Engineering Sciences at the University of Southampton. He is also a director of HiT Systems Ltd. He has published over 60 papers in academic journals and conferences. His main research interests are in the area of electrical machines and drives.

Dr Sharkh is a member of the IEE and a Chartered Engineer.

S. H. Lai obtained his BEng and PhD degrees from the University of Southampton, UK in 2002 and 2006, respectively.

He currently works as a Process Support Engineer with Applied Materials South East Asia Pte Ltd in Singapore.

APPENDIX

The flux distribution in the magnets and the airgap of the machine can be determined by solving the Laplace's and Poisson's equations of the scalar magnetic potentials φ_I and φ_{II} in the airgap and magnets, respectively, as described in [15] and [16],

$$\begin{aligned} \nabla^2\varphi_I &= 0 && \text{in the airgap} \\ \nabla^2\varphi_{II} &= \frac{1}{\mu_r}\nabla.\mathbf{M} && \text{in the magnets} \end{aligned} \tag{A1}$$

where $\mathbf{M}$ is the residual magnetization vector of the magnets and μ_r is the relative recoil permeability of the magnets. The field vector $\mathbf{H}$ can be calculated as

$$\mathbf{H} = -\nabla\varphi \tag{A2}$$

The field vectors $\mathbf{B}$ and $\mathbf{H}$ are coupled by:

$$\mathbf{B_I} = \mu_0\mathbf{H_I} \quad \text{in the airgap} \tag{A3}$$

$$\mathbf{B_{II}} = \mu_0\mu_r\mathbf{H_{II}} + \mu_0\mathbf{M} \quad \text{in the magnets} \tag{A4}$$

In polar coordinates (neglecting end effects variation in the axial *z*-direction) equations (1) can be written as:

$$\frac{\partial^2\varphi_I}{\partial r^2} + \frac{1}{r}\frac{\partial\varphi_I}{\partial r} + \frac{1}{r^2}\frac{\partial^2\varphi_I}{\partial\vartheta^2} = 0 \quad \text{in the airgap} \tag{A5}$$

$$\frac{\partial^2\varphi_{II}}{\partial r^2} + \frac{1}{r}\frac{\partial\varphi_{II}}{\partial r} + \frac{1}{r^2}\frac{\partial^2\varphi_{II}}{\partial\vartheta^2} = \frac{1}{\mu_r}\nabla.\mathbf{M} \quad \text{in the magnets} \tag{A6}$$

For magnets with linear second-quadrant demagnetization characteristics in the, the amplitude of the magnetization vector $\mathbf{M}$ is given by

$$M = \frac{B_r}{\mu_0} \tag{A7}$$

where B_r is the remanent flux density of the magnet. For the parallel-magnetized magnets used in the motor described in this paper, the direction of magnetization is as illustrated in Fig. A1, and the magnetization vector in polar coordinates is given by

$$\mathbf{M} = M_r\mathbf{u}_r + M_\theta\mathbf{u}_\theta \tag{A8}$$

where $\mathbf{u}_r$ and $\mathbf{u}_\theta$ are unit vectors in the r and θ directions respectively, and

$$\left.\begin{aligned} M_r &= \frac{B_r}{\mu_0}\cos\theta \\ M_\theta &= -\frac{B_r}{\mu_0}\sin\theta \end{aligned}\right\} -\alpha\frac{\pi}{2p} \le \theta \le \alpha\frac{\pi}{2p} \tag{A9}$$

$$\left.\begin{aligned} M_r &= 0 \\ M_\theta &= 0 \end{aligned}\right\} \alpha\frac{\pi}{2p} \le \theta \le (2-\alpha)\frac{\pi}{2p} \tag{A10}$$

$$\left.\begin{aligned} M_r &= -\frac{B_r}{\mu_0}\cos\left(\theta - \frac{\pi}{p}\right) \\ M_\theta &= \frac{B_r}{\mu_0}\sin\left(\theta - \frac{\pi}{p}\right) \end{aligned}\right\} (2-\alpha)\frac{\pi}{2p} \le \theta \le \alpha\frac{3\pi}{2p} \tag{A11}$$

$$\left.\begin{aligned} M_r &= 0 \\ M_\theta &= 0 \end{aligned}\right\} \alpha\frac{3\pi}{2p} \le \theta \le \frac{3\pi}{2p} \tag{A12}$$

which can be expressed as a Fourier series [15] by:

$$M_r = \sum_{n=1,3,5...}^{\infty} M_{rn}\cos(np\theta) \tag{A13}$$

$$M_\theta = \sum_{n=1,3,5...}^{\infty} M_{\theta n}\sin(np\theta) \tag{A14}$$

where,

$$M_{rn} = \frac{B_r}{\mu_0}\alpha(A_{1n} + A_{2n}) \tag{A15}$$

$$M_{\theta n} = \frac{B_r}{\mu_0}\alpha(A_{1n} - A_{2n}) \tag{A16}$$

where,

$$A_{1n} = \frac{\sin\left[(np+1)\alpha\frac{\pi}{2p}\right]}{(np+1)\alpha\frac{\pi}{2p}} \tag{A17}$$

$$A_{2n} = \frac{\sin\left[(np-1)\alpha\frac{\pi}{2p}\right]}{(np-1)\alpha\frac{\pi}{2p}} \tag{A18}$$

where α is the ratio of the pole-arc width of a magnet pole over the width of the pole pitch which is equal to $\frac{\pi}{p}$, where p is the number of pole pairs.

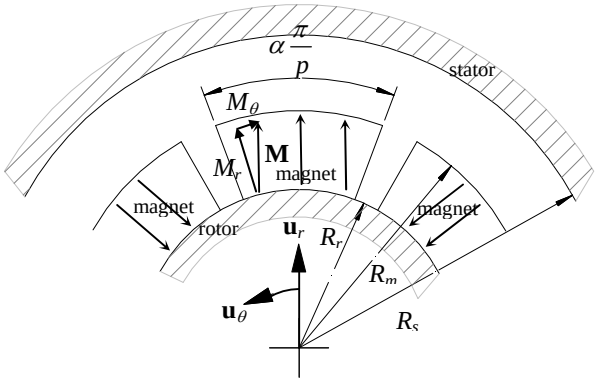

Fig. A1. Motor airgap geometry and coordinate system

The magnetisation source for equation (A6) can now be derived as:

$$\nabla.\mathbf{M} = \frac{M_r}{r} + \frac{\partial M_r}{\partial r} + \frac{1}{r}\frac{\partial M_\theta}{\partial\theta} = \sum_{n=1,3,5...}^{\infty}\frac{1}{r}M_n\cos(np\theta) \tag{A18}$$

where:

$$M_n = M_{rn} + npM_{\theta n} \tag{A19}$$

Assuming infinitely permeable rotor and stator steels, the boundary conditions are given by:

$$\begin{aligned} &H_{\theta I}(R_s,\theta) = 0 \\ &H_{\theta II}(R_r,\theta) = 0 \\ &B_{rI}(R_m,\theta) = B_{rII}(R_m,\theta) \\ &H_{\theta I}(R_m,\theta) = H_{\theta II}(R_m,\theta) \end{aligned} \tag{A20}$$

Solving for these equations yields the solutions for magnetic flux density. In the motor airgap:

$$B_{rI}(r,\theta) = \sum_{n=1,3,5...}^{\infty} K_B(n)\, f_{Br}(r)\cos(np\theta) \tag{A21}$$

$$B_{\theta I}(r,\theta) = \sum_{n=1,3,5...}^{\infty} K_B(n)\, f_{B\theta}(r)\sin(np\theta) \tag{A22}$$

For $np \neq 1$ (considering only motors with more that 2 poles):

$$K_B(n) = \frac{\mu_0 M_n}{\mu_r}\frac{np}{(np)^2-1}\left\{\frac{(A_{3n}-1)+2\left(\frac{R_r}{R_m}\right)^{np+1}-(A_{3n}+1)\left(\frac{R_r}{R_m}\right)^{2np}}{\frac{\mu_r+1}{\mu_r}\left[1-\left(\frac{R_r}{R_s}\right)^{2np}\right]-\frac{\mu_r-1}{\mu_r}\left[\left(\frac{R_m}{R_s}\right)^{2np}-\left(\frac{R_r}{R_m}\right)^{2np}\right]}\right\} \tag{A23}$$

$$f_{Br}(r) = \left(\frac{r}{R_s}\right)^{np-1}\left(\frac{R_m}{R_s}\right)^{np+1}+\left(\frac{R_m}{r}\right)^{np+1} \quad , \quad f_{B\theta}(r) = -\left(\frac{r}{R_s}\right)^{np-1}\left(\frac{R_m}{R_s}\right)^{np+1}+\left(\frac{R_m}{r}\right)^{np+1} \quad \text{and} \quad A_{3n} = \left(np-\frac{1}{np}\right)\frac{M_{rn}}{M_n}+\frac{1}{np} \tag{A24}$$

In the magnets:

$$\begin{aligned} B_{rII} = &\sum_{n=1,3,5...}^{\infty} \mu_0 M_n \frac{np}{(np)^2-1} \\ &\cdot\left\{\frac{\left(A_{3n}-\frac{1}{\mu_r}\right)\left(\frac{R_m}{R_s}\right)^{2np}+\left(1+\frac{1}{\mu_r}\right)\left(\frac{R_r}{R_m}\right)^{np+1}\left(\frac{R_m}{R_s}\right)^{2np}-\left(A_{3n}+\frac{1}{\mu_r}\right)-\left(1-\frac{1}{\mu_r}\right)\left(\frac{R_r}{R_m}\right)^{np+1}}{\frac{\mu_r+1}{\mu_r}\left[1-\left(\frac{R_r}{R_s}\right)^{2np}\right]-\frac{\mu_r-1}{\mu_r}\left[\left(\frac{R_m}{R_s}\right)^{2np}-\left(\frac{R_r}{R_m}\right)^{2np}\right]}\right\} \\ &\cdot\left[\left(\frac{r}{R_m}\right)^{np-1}+\left(\frac{R_r}{R_m}\right)^{np-1}\left(\frac{R_r}{r}\right)^{np+1}\right]\cos(np\theta)+\sum_{n=1,3,5...}^{\infty}\mu_0 M_n\frac{np}{(np)^2-1}\left(\frac{R_r}{r}\right)^{np+1}\cos(np\theta) \\ &+\sum_{n=1,3,5...}^{\infty}\mu_0 M_n\frac{npA_{3n}}{(np)^2-1}\cos(np\theta) \end{aligned} \tag{A25}$$

$$\begin{aligned} B_{\theta II} = &\sum_{n=1,3,5...}^{\infty} -\mu_0 M_n \frac{np}{(np)^2-1} \\ &\cdot\left\{\frac{\left(A_{3n}-\frac{1}{\mu_r}\right)\left(\frac{R_m}{R_s}\right)^{2np}+\left(1+\frac{1}{\mu_r}\right)\left(\frac{R_r}{R_m}\right)^{np+1}\left(\frac{R_m}{R_s}\right)^{2np}-\left(A_{3n}+\frac{1}{\mu_r}\right)-\left(1-\frac{1}{\mu_r}\right)\left(\frac{R_r}{R_m}\right)^{np+1}}{\frac{\mu_r+1}{\mu_r}\left[1-\left(\frac{R_r}{R_s}\right)^{2np}\right]-\frac{\mu_r-1}{\mu_r}\left[\left(\frac{R_m}{R_s}\right)^{2np}-\left(\frac{R_r}{R_m}\right)^{2np}\right]}\right\} \\ &\cdot\left[\left(\frac{r}{R_m}\right)^{np-1}-\left(\frac{R_r}{R_m}\right)^{np-1}\left(\frac{R_r}{r}\right)^{np+1}\right]\sin(np\theta)+\sum_{n=1,3,5...}^{\infty}\mu_0 M_n\frac{np}{(np)^2-1}\left(\frac{R_r}{r}\right)^{np+1}\sin(np\theta) \\ &-\sum_{n=1,3,5...}^{\infty}\mu_0 M_n\frac{A_{3n}}{(np)^2-1}\sin(np\theta) \end{aligned} \tag{A26}$$